Int. J. Electrochem. Sci., 15 **(2020)** 9769 – 9778, doi: 10.20964/2020.10.60

International Journal of ELECTROCHEMICAL SCIENCE
www.electrochemsci.org

Electrochemical Mechanism of Microporous Autocatalytic Surface Formation on a High-Chromium Alloy in an Alkaline Solution

Fulin Zhang[1], *Zhuji Jin*[1,*], *Lida Wang*[2], *Guannan Jiang*[1], *Junmin Pei*[1]

[1] Key Laboratory for Precision and Non-Traditional Machining Technology of Ministry of Education, Dalian University of Technology, Dalian 116024, PR China
[2] Department of Chemical Engineering, School of Chemical Engineering, Dalian University of Technology, Dalian 116024, PR China
[*]E-mail: kimsg@dlut.edu.cn

Received: 25 June 2020 / *Accepted:* 13 August 2020 / *Published:* 31 August 2020

An experimental and analytical investigation of the formation of a microporous layer of mixed ferric oxide and ferric hydroxide on a high-chromium alloy in alkaline solution under the oxygen evolution region is presented. By potentiostatic polarization under 5 $V_{Ag/AgCl}$, a dark red microporous layer was formed on the surface of the high-chromium alloy. The workpieces and electrolytes were examined and analyzed by scanning electron microscopy (SEM), X-ray fluorescence (XRF), Raman microscopy (RMS) and inductively coupled plasma (ICP) to probe the electrochemical mechanism of layer formation. The results demonstrate that under the set conditions, Fe(VI) ions were generated from the anode. However, due to the consumption of OH^- ions, Fe(VI) ions were decomposed into ferric hydroxide; in turn, ferric hydroxide had an autocatalytic effect on the decomposition of Fe(VI) ions. The anodic reaction steps were controlled by the mass transfer of OH^- ions, and alternative transformation between Fe(VI) ions and ferric hydroxide accelerated the formation of a microporous layer.

Keywords: High-chromium alloy; Autocatalytic effect; Anodic reactions; Electrochemical deposition

1. INTRODUCTION

The rapid development of the nuclear power industry has increased demands for durable and high-temperature alloys. High-chromium alloys with high corrosion and high temperature resistance are widely used as nuclear materials [1-3]. However, traditional machining of high-chromium alloys causes serious tool wear and high machining force due to their high hardness. Electrochemical abrasive machining (ECAM) is a nontraditional machining method combining electrochemical pretreatment and further mechanical machining [4,5]. The microporous structure is formed through electrochemical dissolution before being removed by mechanical methods. Compared with that of the original material,

the mechanical strength of materials made with ECAM is significantly decreased due to the formation of a microporous structure [6,7]. Thus, ECAM has the advantages that any conductive material can be machined with low machining force and tool wear regardless of its hardness [8].

A microporous structure with a thickness of a few micrometers should be formed within seconds to balance the mechanical effect; however, excessive corrosion should also be avoided to meet machining precision. The electrochemical behavior of Cr-Fe alloys in different electrolytes has been investigated by researchers in recent years [9-13]. Passive films on the surface of Cr-Fe alloys are easily formed in an extremely short time in neutral and diluted acidic electrolytes (usually $NaNO_3$, $NaClO_3$ and diluted H_2SO_4 solution). However, the passive film is usually a few nanometers thick, which is undesirable in ECAM. By contrast, the breakdown of passive film by halide ions in neutral electrolytes (usually Cl^- or F^- ions) accelerates the continuous dissolution of materials, resulting in serious stray corrosion. Thus, neither neutral nor acidic electrolytes are suitable for the ECAM of high-chromium alloys. According to the potential-pH diagram [14], dissolved metal ions may tend to form a hydroxide film on the anode surface in solutions with high concentrations of OH^- ions. Compared with the passive film, the hydroxide film can reach a thickness of several micrometers, and the film may have an effect on avoiding excessive corrosion. Thus, alkaline electrolytes are considered to be suitable for the ECAM of high-chromium alloys. To date, there have been no studies on the electrochemical behavior of high-chromium alloys in alkaline solutions.

Here, the electrochemical behavior of a high-chromium alloy in an alkaline solution under the potential of the oxygen revolution region was investigated. A dark red layer with a microporous structure was formed on the anode surface after polarization. The microstructure, evolution of elements and composition of the formed microporous layer were studied by a series of detection methods. As a result, the electrochemical deposition mechanism of the microporous autocatalytic layer is clearly revealed.

2. EXPERIMENT

2.1 Workpiece preparation

The high-chromium alloy used in this paper was cast for nuclear reactor cladding. The composition of the alloy is listed in Table 1. Before the electrochemical experiments, the workpieces (13 mm×13 mm×5 mm) were ground with successive SiC abrasive papers up to grit P2000, cleaned by anhydrous ethanol in an ultrasonic environment and finally dried.

Table 1. Chemical composition of high-chromium alloy

Element	Cr	Fe	Ni	Mo	Cu	C	Si	S, P, V etc.
Concentration (wt.%)	≈40	40	≈6.5	≈4	≈1.5	≈1.5	≈1	≈5.5

2.2 Electrochemical measurement

A Parstat 2273 advanced electrochemical system with a three-electrode cell (300 ml) was used for electrochemical measurements. A platinum net (30 mm × 30 mm) was used as the counter electrode and Ag/AgCl in 3.5 M KCl solution as the reference electrode (+205 mV vs. a standard hydrogen electrode (SHE) at 25 °C). An amount of 300 ml of 1 M NaOH solution was used as the electrolyte. A total of 180 s of potentiostatic polarization at -1.5 $V_{Ag/AgCl}$ was carried out before potentiodynamic polarization to remove the oxide film. Potentiodynamic polarization was carried out from -2 $V_{Ag/AgCl}$ to 6 $V_{Ag/AgCl}$ with a scanning rate of 0.5 $mV \cdot s^{-1}$ at 25 °C. Potentiostatic polarization was carried out at 0.5 $V_{Ag/AgCl}$ and 5 $V_{Ag/AgCl}$ for 200 s.

The microstructure and composition after polarization were tested by scanning electron microscopy (FEI, Quanta 450) with an energy-dispersive spectrometer (EDS). Macroscopic and quantitative analyses of polarized workpieces were carried out by X-ray fluorescence (XRF, Shimadzu XRF 1800). The polarization product on the anode surface was tested by Raman microscopy (Thermo Fisher Scientific DXR). The concentrations of Cr and Fe ions in the solutions were tested by inductively coupled plasma (ICP, Perkinelmer Optima 2000DV). The section view of the microporous layer was observed by a superhigh magnification lens zoom 3D microscope (Keyence VHX 600E).

3. RESULTS AND DISCUSSION

3.1 Surface morphology

The polarization curve of the high-chromium alloy is plotted in Fig. 1a. From the polarization curve between -2 and 6 $V_{Ag/AgCl}$, passive, transpassive and oxygen evolution regions are clearly observed. Based on Faraday's law, a higher current density represents a higher reaction rate, which is desirable for ECAM [15]; thus, 5 $V_{Ag/AgCl}$ was selected for the experiment, while 0.5 $V_{Ag/AgCl}$ was selected for comparison. The digital images of the polarized areas of the workpiece are shown in Fig. 1(b, e). It is clear that after being polarized for 200 s under 0.5 and 5 $V_{Ag/AgCl}$, a dark red layer was observed on the alloy surface. The much darker layer formed under 5 $V_{Ag/AgCl}$ covered the polarized area completely. The potentiostatic polarization curves are plotted in Fig. 1(c, f). Generally, the current density is derived mainly from two types of electrochemical reactions: dissolution of metal and electrolysis of water. Since there were hardly any bubbles observed near the anode under both selected potentials, the electrolysis of water can be ignored in this experiment. Under 0.5 $V_{Ag/AgCl}$, the current density was extremely low with a peak value of 10 mA, while it was relatively high with a peak value of approximately 0.54 A under 5 $V_{Ag/AgCl}$, indicating that the reaction rate of the metal is higher under the high potential than under the low potential. It is intriguing that under 5 $V_{Ag/AgCl}$, significant current oscillation was observed. During polarization, there was no precipitation observed in the electrolyte, and the phenomenon was considered to be related to the electrochemical mechanism, which will be discussed in the following section. Fig. 1(d, g) shows the SEM images of the polarized area. The microporous structure formed on the surface under both selected potentials, while at 5 $V_{Ag/AgCl}$, the structure was much looser. As a result,

5 $V_{Ag/AgCl}$ was suitable for ECAM of high-chromium alloy.

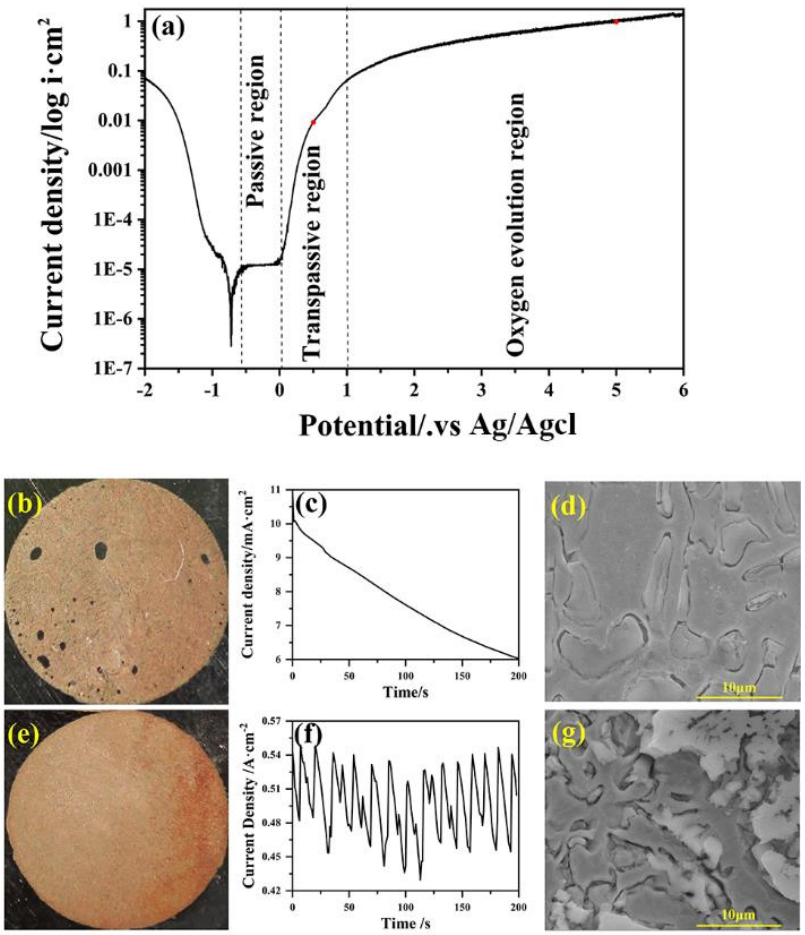

Figure 1. Polarization curve of high-chromium alloy (a). Digital images of the polarized area at 0.5 $V_{Ag/AgCl}$ (b) and 5 $V_{Ag/AgCl}$ (e). Current density curves at 0.5 $V_{Ag/AgCl}$ (c) and 5 $V_{Ag/AgCl}$ (f). The microstructure of the polarized area at 0.5 $V_{Ag/AgCl}$ (d) and 5 $V_{Ag/AgCl}$ (g).

3.2 Composition of the layer

EDS is one of the most common methods to detect surface elements. The EDS test of the original surface and polarized areas under 5 $V_{Ag/Agcl}$ in 1 M NaOH for 200 s are listed in Table 2. Compared to the original surface, an Fe-rich layer formed since the Fe content was raised to 40.97 wt.%, while the Cr content decreased to 18.45 wt.%. In addition, the O content was raised to 22.45 wt.%, which indicates that metal oxides formed on the polarized area.

Table 2. Main chemical composition of the original surface and polarized area

Element	Fe (wt.%)	Cr (wt.%)	O (wt.%)
Original surface	35.86	42.07	-
Polarized area	40.97	18.45	22.45

It should be noted that EDS can only produce microanalytical results of relative quantifiable elemental composition and is not a surface sensitive technique. Therefore, these data should be considered indicative but do not allow for general trends to be noted. XRF was used for further macroscopic and quantitative analysis. To study the variation in elements versus polarization time and polarized area, potentiostatic polarization was carried out under 5 $V_{Ag/AgCl}$ from 15 to 120 s with an increment of 15 s. It is shown in Fig. 2a that the Fe content in the polarized area was approximately 47 wt.% with little change during polarization, while the Cr content gradually decreased to 30.88 wt.%. In addition, the O content increased to 9.38 wt.% rapidly in the first 15 s and then increased slowly to 14.79 wt.%.

A Raman spectrometer was used to determine the composition of the dark red layer formed on the polarized area. The workpiece was polarized under 5 $V_{Ag/Agcl}$ for 200 s and then dried before testing. As shown in Fig. 2b, two main peaks were clearly observed at 519 and 693 cm^{-1}. According to reference [16], it seems clear that the first peak at 519 cm^{-1} can be confidently assigned to γ-Fe_2O_3 and the second peak at 693 cm^{-1} was considered to be $Fe(OH)_3$. Since no Cr oxide or hydroxide peaks were detected and Cr in the polarized area decreased according to XRF, it seems that Cr involved in anodic reactions was dissolved into the electrolyte rather than deposited onto the anode.

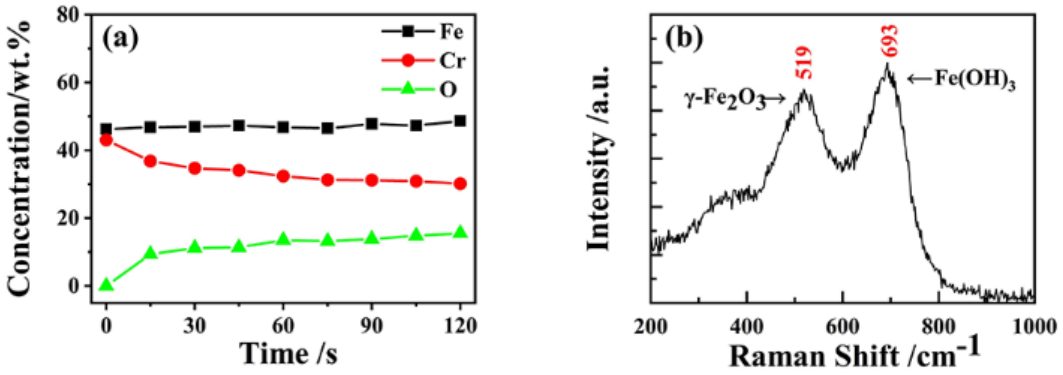

Figure 2. Concentration of the main elements in the polarized area (a), Raman spectrum of the polarized area (b).

3.3 Fe and Cr elements in the electrolyte and microporous layer

The Fe and Cr elements involved in the anodic reactions were mainly dissolved into the electrolyte or deposited onto the anode surface. To trace elements involved in anodic reactions, ICP was used to detect metal ions in solution. The workpieces were polarized under 5 $V_{Ag/AgCl}$ for 120 s, and samples were collected every other 15 s. As shown in Fig. 3a, the electrolyte contains Cr ions but no Fe ions. The Cr ion concentration increased to 0.81 $mg \cdot L^{-1}$ rapidly in the first 15 s and then gradually increased to 1.49 $mg \cdot L^{-1}$ from 15 to 120 s. The results indicate that Fe involved in the anodic reaction was deposited onto the anode surface, and the dissolution rate of Cr was relatively low after 15 s.

The substrate is insoluble in dilute acid, while the microporous layer, which is mainly composed of deposited metal oxides or hydroxides, is soluble. Therefore, 30 ml of dilute nitric acid was used to

immerse the polarized workpieces and dissolve the microporous layer, and then the samples were collected for ICP analysis. Using this method, the concentrations of ions detected represent the elemental contents of the microporous layer. It is shown in Fig. 3b that no Cr ions were detected in the collected samples, while the concentration of Fe ions increased to 5.5 $mg \cdot L^{-1}$ in the first 15 s and then fluctuated around the value of 5 $mg \cdot L^{-1}$. The results show that ferric oxide and hydroxide are the main components in the microporous layer. After 15 s, Fe in the inner substrate was prevented from reacting with the electrolyte since it can be calculated from Fig. 3b that the total amount of Fe involved in anodic reactions remained nearly unchanged after 15 s.

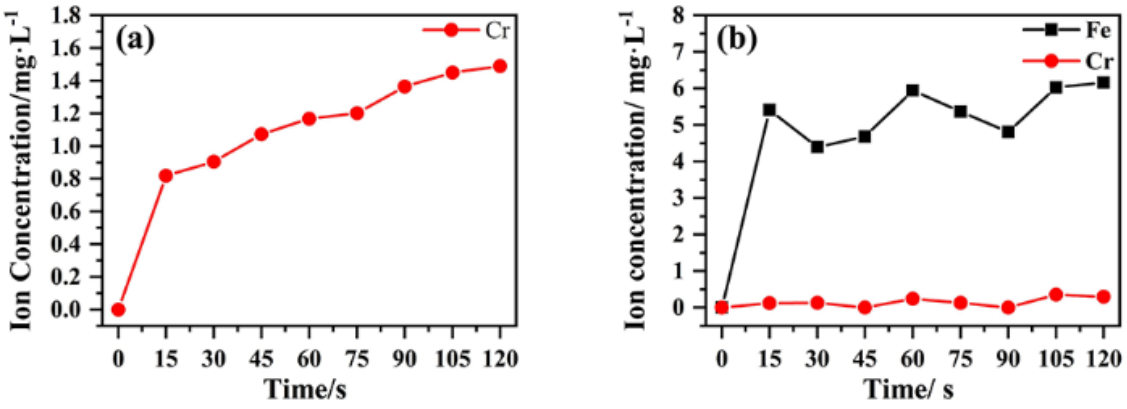

Figure 3. Concentration of Fe and Cr ions in the electrolyte (a) and Fe and Cr ions in the collected samples

3.4 Thickness of the microporous layer

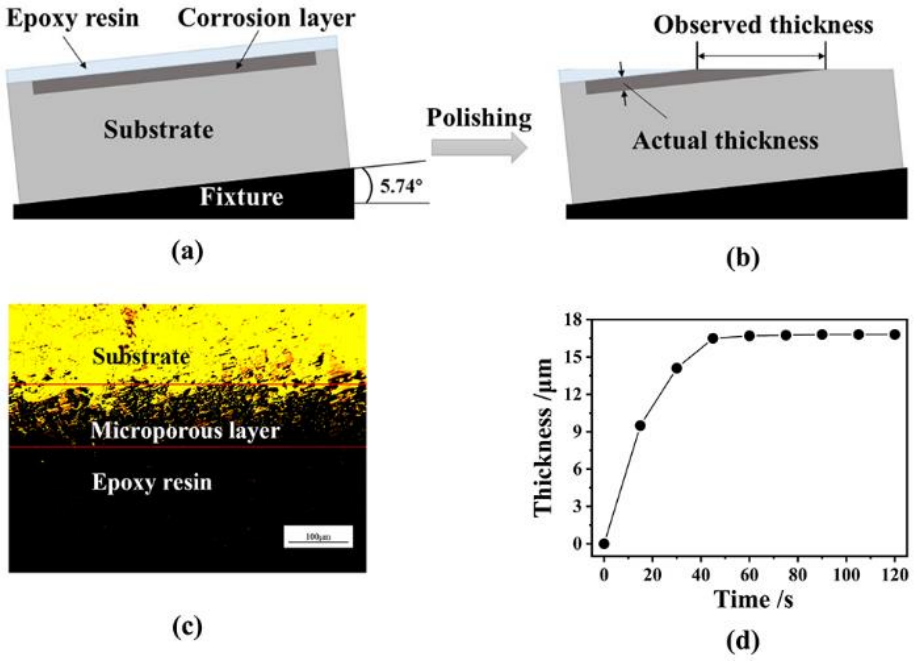

Figure 4. Angle-polishing method (a, b), angle section-view digital image of microporous layer (c), the thickness of the microporous layer (d).

The formation of microporous structures with thicknesses of several micrometers is crucial for the ECAM of high-chromium alloys. To measure the thickness accurately, the cross section was magnified by the angle-polishing method, as shown in Fig. 4 (a, b). A superhigh magnification lens zoom 3D microscope was used to measure the thickness of the microporous layer after angle polishing. An angle section-view digital image is shown in Fig. 4c. Using this method, the actual thickness of the layer was calculated and is shown in Fig. 4d. After polarization for 15 s, the thickness of the microporous layer was approximately 10 μm, and after 45 s, the thickness stabilized at approximately 17 μm. The results indicate that the thickness of the microporous layer is controllable, which is desirable for precision machining. Since it only takes 15 s to form a layer with a thickness of 10 μm, the efficiency of further mechanical machining is guaranteed.

3.5 Electrochemical Mechanism of the formation of the microporous layer

Current oscillations can provide significant information on the fundamental mechanisms of the electrochemical process. The occurrence of current oscillation is that with the field drives the electrochemical system from equilibrium, the effect of nonlinear terms becomes significant [17]. The selected experimental potential was 5 $V_{Ag/AgCl}$; however, as shown in Fig. 1.a, the equilibrium electrode potential of a high-chromium alloy is -0.7 $V_{Ag/AgCl}$, which is much lower than the applied potential. As a result, the electrochemical system was far from equilibrium. Studies have shown that current oscillation is often related to complicated electrochemical processes, such as adsorption/desorption, coordination, pitting, formation/dissolution of the oxide layer and reduction of inorganic molecules and ions [18-24]. During the experiment, a layer of mixed ferric oxide and ferric hydroxide was formed on the surface of the high-chromium alloy. According to Fig. 3b, the total amount of Fe involved in the anodic reaction remained unchanged after 15 s; however, it is clear that based on Fig. 1f, the current oscillation continued throughout the whole process. The comparison between Fig. 3b and Fig. 1f indicates that after 15 s, the relatively high current density was due to the dissolution of ferric oxide and ferric hydroxide. As a consequence, under the experimental conditions of a 1 M NaOH solution as the electrolyte and potentiostatic polarization under 5 $V_{Ag/AgCl}$, the current oscillation was mainly derived from the alternate formation/dissolution of ferric oxide and ferric hydroxide.

To reveal the mechanism of the formation of the microporous layer, a qualitative model shown in Fig. 5 can be assumed to illustrate the electrochemical behavior of the high-chromium alloy under high potential in solution with a high concentration of OH^- ions. According to the potential-pH diagram of Fe-H_2O and Cr-H_2O systems[14], Fe tends to be dissolved to Fe(VI) ions, while Cr tends to be dissolved to Cr(VI) ions under high potential and high pH values. Fe^{n+} and Cr^{n+} ions tend to bond with OH^- ions to form precipitates in the electrolyte. Since there was no precipitation observed during the whole process, it is clear that there were no Fe^{n+} and Cr^{n+} ions generated during anodic reactions. As shown in Fig. 5a, etching pits were formed on the surface of the anode due to the initial dissolution of Cr and Fe. The first reaction step is listed in Eqs. (1-2):

$$Cr + 8OH^- \rightarrow CrO_4^{2-} + 4H_2O + 6e^- \quad (1)$$

$$Fe + 8OH^- \rightarrow FeO_4^{2-} + 4H_2O + 6e^- \quad (2)$$

FeO_4^{2-} and CrO_4^{2-} ions carry a negative charge, both of which accumulate in the formed pits. In the early stage, a large number of OH^- ions were consumed due to reaction (1-2), while the diffusion rate of OH^- was limited in the electrolyte. The chemistry and reactivity of Fe(VI) ions highly depend on the concentration of OH^- ions, and they spontaneously self-decay in the presence of water at relatively low pH values to form ferric hydroxide, hydrogen peroxide and oxygen. The second reaction step is listed in Eqs. (3-8) [25]:

$$FeO_4^{2-} + FeO_4^{2-} \rightarrow [FeO_4\ FeO_4]^{4-} \quad (3)$$

$$[FeO_4\ FeO_4]^{4-} + 4\ H_2O \rightarrow 2\ FeO_4^{4-} + 2H_2O_2 + 4H^+ \quad (4)$$

$$FeO_4^{4-} + H_2O_2 + 4H^+ \rightarrow Fe(OH)_2 + O_2 + 2H_2O \quad (5)$$

$$FeO_4^{2-} + Fe(OH)_2 + H_2O \rightarrow FeO_4^{3-} + Fe(OH)_3 + H^+ \quad (6)$$

$$FeO_4^{3-} + H_2O + 3\ H^+ \rightarrow Fe(OH)_3 + H_2O_2 \quad (7)$$

$$FeO_4^{3-} + H_2O_2 + 3H^+ \rightarrow Fe(OH)_3 + O_2 + H_2O \quad (8)$$

The self-decay product ferric hydroxide has an autocatalytic effect on the decomposition of Fe(VI) ions [26,27]. Therefore, the polarized area was covered by an autocatalytic layer of $Fe(OH)_3$ in a short time, as shown in Fig. 5b. It is necessary to mention that the γ-Fe_2O_3 detected on the polarized area by Raman spectroscopy was formed by dehydration of $Fe(OH)_3$ during the drying process before testing. Under the potential of 5 $V_{Ag/AgCl}$, the formed $Fe(OH)_3$ layer was not stable due to the replenishment of OH^- ions by mass transfer, as shown in Fig. 5c. The $Fe(OH)_3$ layer was oxidized to FeO_4^{2-} ions again, and the third reaction step is listed in Eqs (4):

$$Fe(OH)_3 + 5OH^- \rightarrow FeO_4^{2-} + 4H_2O + 3e^- \quad (9)$$

After that, reactions (3-8) dominated again since the OH^- ions near the anode surface were largely consumed by reaction (9), while the concentration of FeO_4^{2-} ions increased. As a consequence, the reaction of Fe during the anodic process can be briefly explained as an alternative transformation between FeO_4^{2-} ions and the $Fe(OH)_3$ autocatalytic layer. Due to the periodic formation and dissolution of the $Fe(OH)_3$ layer, the resistance of the anode changed rapidly, resulting in current oscillation, as shown in Fig. 1f. Due to the autocatalytic effect of ferric hydroxide, the FeO_4^{2-} ions were consumed to form an $Fe(OH)_3$ autocatalytic layer before diffusing into the electrolyte. Therefore, no soluble Fe ions were detected in the electrolyte by ICP. During the whole anodic process, before the $Fe(OH)_3$ autocatalytic layer was completely dissolved by the third step, the second step dominated again, thus inhibiting the reaction of the inner Fe element. This indicates that after the alternative transformation between FeO_4^{2-} and $Fe(OH)_3$ reached a dynamic equilibrium, the total amount of Fe involved in the reaction was unchanged. This indication is in line with the findings shown in Fig. 3b that after 15 s, the Fe content in the microporous layer remained relatively stable.

Cr was continuously oxidized to CrO_4^{2-} ions. In the early stage, the dissolution rate of Cr was fast. However, the subsequently formed autocatalytic layer covered the inner substrate, which made the transfer of CrO_4^{2-} ions from the substrate to the electrolyte harder than in the early stage; thus, the dissolution rate of Cr was inhibited. The continuous dissolution of Cr caused the microporous autocatalytic layer to become looser, which is desirable for further machining processes.

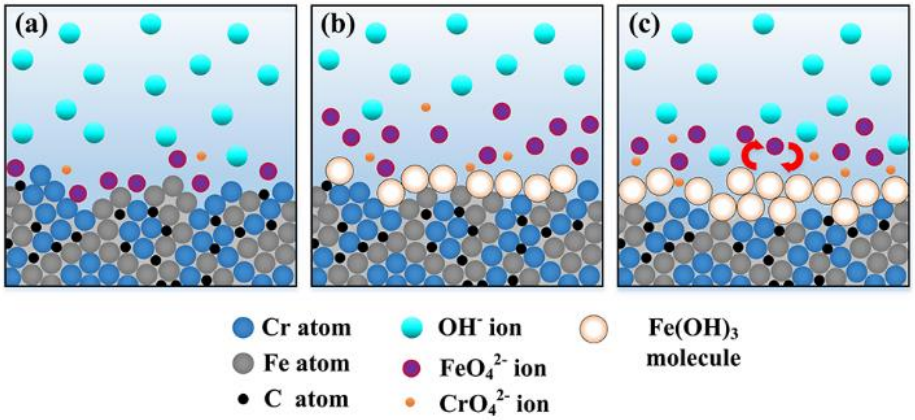

Figure 5. Qualitative model of the electrochemical behavior of high-chromium at 5 $V_{Ag/AgCl}$ in 1 M NaOH solution

4. CONCLUSION

This paper investigated the microporous autocatalytic layer formed on a high-chromium alloy in NaOH solution under a relatively high potential. The following conclusions can be drawn:

1. A microporous autocatalytic layer is formed by potentiostatic polarization under 5 $V_{Ag/AgCl}$ in 1 M NaOH solution;
2. The alternative transformation between Fe(VI) ions and ferric hydroxide, which is controlled by the mass transfer of OH^-, dominates the formation of the autocatalytic layer. Due to the autocatalytic effect of ferric hydroxide on the decomposition of Fe(VI), the anodic reactions reach dynamic equilibrium soon after 15 s, making the thickness of this autocatalytic layer controllable; and
3. The autocatalytic layer with a microporous structure that can be easily removed by mechanical force is suitable for precision machining.

An electrochemical treatment method was proven suitable for the ECAM of high-chromium alloys. How other factors, such as temperature and flow field, influence the machining precision during ECAM will be studied in our future work.

ACKNOWLEDGMENTS
The authors would like to thank the financial support from the National Key Basic Research and Development Program, No. 2015CB057304, the Science Challenge Project, No. TZ2016006-0103， No. TZ2016006-0107-02, and the Science Fund for Creative Research Groups of NSFC, No.51621064. The authors would also like to extend sincere thanks to all project staff and researchers.

References

1. T. Cheng, J. R. Keiser, M. P. Brady, K. A. Terrani, B. A. Pint, *J. Nucl. Mater.*, 427 (2012) 396
2. R. L. Klueh, *Int. Mater. Rev.*, 50, (2013) 287
3. P. Yvon, F. Carré, *J. Nucl. Mater.*, 385, (2009) 217

4. J. C. Hoogvliet, M. Dijksma, B. Kamp, W. P. Van Bennekom, *Anal. Chem.*, 72 (2000) 2016
5. D. T. Curtis, S. L. Soo, D. K. Aspinwall, C. Sage, *CIRP Ann-Manuf. Techn.*, 58 (2009) 173
6. Y. C. Ge, Z. W. Zhu, D. Y. Wang, Z. Ma, D. Zhu, *J. Mater. Process. Tech.*, 271 (2019) 510
7. Q. X. He, Z. J. Jin, G. N. Jiang, Y. Shi, *Mater. Manuf. Process.*, 33 (2018) 1661
8. A. Hasçalık, U. Çaydaş, *J. Mater. Process. Tech.*, 190 (2007) 173
9. D. Y. Wang, Z. W. Zhu, N. F. Wang, D. Zhu, H. R. Wang, *Electrochim. Acta*, 156 (2015) 301
10. S. Ayyappan, K. Sivakumar, *Int. J. Adv. Manuf. Tech.*, 75 (2014) 479
11. S. Ayyappan, K. Sivakumar, *P. I. Mech. Eng. B-J. Eng.*, 229 (2014) 1984
12. B. H. Kim, C. W. Na, Y. S. Lee, D. K. Choi, C. N. Chu, *CIRP Ann-Manuf. Techn.*, 54 (2005) 191
13. T. Massoud, V. Maurice, L. H. Klein, P. Marcus, *J. Electrochem. Soc.*, 160 (2013) C232
14. H. X. You, H. B. Xu, Y. Zhang, S. L. Zheng, Y. Y. Gao, *T. Nonferr. Metal. Soc.*, 20 (2010) s26
15. D. Wu, R. K. Kang, J. Guo, Z. T. Liu, C. Wan, Z. J. Jin, *Electrochem. Commun.*, 103 (2019) 48
16. J. Gui, T. M. Devine, *Corros. Sci.*, 37 (1995) 1177
17. L. F. Ding, P. Wu, J. Cheng, Y. L. Niu, Z. W. Song, X. P. Kong, *Electrochemistry*, 87 (2019) 14
18. C. M. Sulyma, D. Roy, *Corros. Sci.*, 52 (2010) 3086
19. D. Sazou, *Electrochim. Acta*, 42 (1997) 627
20. Z. L. Li, T. H. Wu, Z. J. Niu, W. Huang, H. D. Nie, *Electrochem. Commun.*, 6 (2004) 44
21. F. Raspel, M. Eiswirth, *J. Phys. Chem.*, 98 (1994) 7613
22. M. Pagitsas, A. Diamantopoulou, D. Sazou, *Electrochim. Acta*, 47 (2002) 4163
23. N. I. Potkonjak, Z. Nikolić, S. R. Anić, D. M. Minić, *Corros. Sci.*, 83 (2014) 355
24. S. Y. Zhao, S. H. Chen, H. Y. Ma, D. G. Li, F. J. Kong, *J. Appl. Electrochem*, 32 (2002) 231
25. Y. Lee, R. Kissner, U. Von Gunten, *Environ. Sci. Technol.*, 48 (2014) 5154
26. J. Zhao, Y. Liu, Q. Wang, Y. Fu, X. Lu, X. Bai, *Sep. Purif. Technol.*, 192 (2018) 412
27. Y. Jiang, J. E. Goodwill, J. E. Tobiason, D. A. Reckhow, *Environ. Sci. Technol.*, 49 (2015) 2841